Received: 17 October 2023 | Revised: 15 November 2023 | Accepted: 23 December 2023

DOI: 10.1002/bte2.20230057

RESEARCH ARTICLE

BATTERY ENERGY Open Access WILEY

A novel potassium-containing layered oxide for the cathode of sodium-ion batteries

Manuel Aranda | **Pedro Lavela** | **José L. Tirado**

Departamento de Química Inorgánica e Ingeniería Química, Grupo PAIDI FQM288, Instituto Químico para la Energía y el Medioambiente, Edificio Marie Curie, Córdoba, España

Correspondence
José L. Tirado, Departamento de Química Inorgánica e Ingeniería Química, Grupo PAIDI FQM288, Instituto Químico para la Energía y el Medioambiente, Edificio Marie Curie, planta 1, Campus de Rabanales, 14071 Córdoba, España.
Email: iq1ticoj@uco.es

Funding information
European Union "NextGenerationEU" /PRTR, and the Junta de Andalucía (group FQM288), IQUEMA and SCAI (UCO); project PLEC2021-007779; MCIN/AEI/10.13039/501100011033

Abstract

Layered oxides are successful cathode materials for sodium-ion batteries. Many of these oxides show interesting kinetic behavior but have poor structural stability. To overcome this limitation, an alternative material containing potassium in the interlayer space in trigonal prismatic coordination is studied here. The transition-metal layers are formed by sustainable transition elements such as iron and manganese. The solid was prepared using a sol–gel procedure that led to a product with relatively high purity, with a P′3-type structure indexable in the C2/*m* space group of the monoclinic system. Its electrochemical behavior was studied in sodium metal half-cells. When the cell is charged up to 4.3 V, it is observed that the potassium extraction is not complete. The subsequent discharge of the cell is associated with the intercalation of sodium from the electrolyte. Thus, it is possible to incorporate a greater number of alkaline ions than those extracted in the previous charge. The residual potassium in the structure was found to be favorable to maintaining the structural integrity of the compound upon cycling. This can be explained by the beneficial effect of potassium, which would act as a structural "pillar" in the interlayer, which would reduce structural degradation during cycling.

KEYWORDS
cathode material, sodium-ion batteries

1 | INTRODUCTION

Sodium-ion batteries (SIBs) are currently being developed either as an alternative or as a complement to lithium-ion batteries (LIBs) due to the abundance and low cost of sodium compared to lithium. Cathode materials consisting of layered oxides are particularly promising due to their high energy density, good cyclability, and low cost.[1,2] Structurally, they are similar to those used in LIBs, but with adjustments made to accommodate the larger size of the sodium ions. The most studied, P2-$Na_{2/3}TO_2$ (T: transition metals), have shown promising kinetic behavior, but have low capacity and poor structural stability.[3] To circumvent these problems, other layered cathode materials with potassium in the interlayer and sustainable transition elements such as Fe and Mn have been explored in SIBs. Thus, Wang et al.[4] suggested that the presence of potassium in the sodium layer could act as a pillar to favor sodium-ion transport. In this way, Wang et al.[5]

studied P2-$K_{0.7}Fe_{0.5}Mn_{0.5}O_2$ in sodium half-cells, which showed excellent electrochemical performance in terms of high capacity and cycling stability. However, Mortemard de Boisse et al.[6] group showed that P2-$Na_xMn_{1/2}Fe_{1/2}O_2$ undergoes a phase transition at the end of the discharge, which could jeopardize its stability. On the other hand, Liu et al.[7] studied the monoclinic P3-type $K_{0.45}Mn_{1-x}Fe_xO_2$ series for $x \leq 0.5$ versus potassium and found superior cyclic stability and rate capability, which was attributed to the highly stable layered structure of $K_{0.45}Mn_{0.8}Fe_{0.2}O_2$ material. Other potassium-containing materials were also examined in the literature as potential cathodes in SIBs. Wang et al.[8] found that the P3-type $K_{0.33}Co_{0.53}Mn_{0.47}O_2{\cdot}0.39H_2O$ material could be used for both the anode and the cathode of SIBs. More recently, the use of P2-$Na_{0.612}K_{0.056}MnO_2$ induced a particularly high specific capacity of 240.5 mAh g^{-1}.[9] Here, we extend this previous knowledge to a novel phase and low iron content, $K_{0.4}[Fe_{0.2}Mn_{0.8}]O_2$ with a monoclinic structure, in sodium batteries. Also, the role of residual potassium in the stability of the electrode and the effects of starting charge or discharge on the cycling performance are unveiled.

2 | EXPERIMENTAL SECTION

The synthesis of the compound with the nominal composition of $K_{0.4}[Fe_{0.2}Mn_{0.8}]O_2$ was carried out using a sol–gel method based on citric acid as previously reported.[10] After mixing aqueous solutions of stoichiometric values of potassium, iron, and manganese acetates, and 5% excess potassium bicarbonate, citric acid (in a 3:2 molar ratio) was added. Then, the solution was stirred for 1 h at room temperature and 1.5 h at 200°C in an ethylene glycol bath. The resulting gel was dried at 120°C for 24 h and precalcined at 400°C in the air for 2 h to decompose the acetate groups and release water. Then, the powdered precursor was ground, pelletized, and finally calcined at 900°C for 12 h under an air atmosphere to obtain the raw material.

A sequential wavelength-dispersive X-ray fluorescence (XRF) spectrometer (ZSX Primus IV de Rigaku) was used for the analysis of the chemical composition of samples. X-ray powder diffraction (XRD) was carried out using a Bruker D8 Discover A25 apparatus (Cu Kα radiation, Ge monochromator, and Lynxeye detector). The patterns of raw samples were scanned between 2 and 90 (°2θ) (step size: 0.04° and 672 s per step). TOPAS v.4.2 software was used to calculate the structural parameters. Field-emission, high-resolution transmission electron microscopy (HRTEM) was carried out in a TALOS F200i. Fourier transforms of high-resolution images were indexed using CrystBox software.[11] The X-ray photoelectron spectra (XPS) were measured in a SPECS Phobios 150 MCD spectrometer using an Al Kα source. Before the recordings, the samples were outgassed overnight at a high vacuum. The binding energy calibration was carried out using the C1s line of the adventitious carbon at 284.6 eV as a reference.

For the electrochemical experiments, the synthesized material was used as the working electrodes in Swagelok™-type sodium half-cells. For this purpose, a mixture containing active material (75%), carbon black (15%), and polyvinylidene fluoride (10%) was blended in *N*-methyl-2-pyrrolidone for 2 h to obtain a homogeneous slurry. This paste was then spread onto a 9 mm aluminum disk and vacuum-dried at 120°C for several hours. The working electrodes had a mass loading of ca. 3 mg cm^{-2}. The electrolyte solution was 1M $NaClO_4$ in propylene carbonate (PC) and 2% fluoroethylene carbonate (FEC), which was soaked in glass fiber separators (GF/A-Whatman). The electrochemical cells were assembled in an argon-filled MBraun glovebox under controlled O_2 and H_2O traces to perform voltammetric, galvanostatic, and impedance spectroscopy experiments. The electrodes were studied at different current densities with potentials between 1.5 and 4.3 V. Electrochemical impedance spectroscopy (EIS) was performed between 1 mHz and 1 MHz. Cyclic voltammetry (CV) with scan rates between 0.1 and 1.0 mV s^{-1} was also performed in the 1.5–4.3 V potential window.

3 | RESULTS AND DISCUSSION

The chemical composition of the compound prepared by sol–gel synthesis[8] was checked by XRF. These results correspond to a $K_{0.42}[Fe_{0.17}Mn_{0.83}]O_2$ formula, in good correspondence with the nominal stoichiometry, and manganese in the 3.7+ average oxidation state. This oxidation state prevents the undesirable Jahn–Teller distortion.[12] In contrast to previous reports,[5,7] the solid adopted the monoclinic structure of P′3-$K_{0.8}CrO_2$, with potassium in trigonal prismatic coordination, an interesting material for potassium-ion batteries.[13] The XRD patterns (Figure S1) reveal a high-purity phase. Thus, Rietveld analysis of XRD data using the C2/*m* space group yielded the unit cell parameters $a = 0.5099_3$ nm, $b = 0.2864_5$ nm, $c = 0.7130_3$ nm, y and $\beta = 102.22_4°$ (Table 1). The fitted structure is shown in Figure 1 and the refined crystallographic parameters are shown in the supporting Information file, Table S1.

HRTEM images of the particles show crystalline domains in the 40–60 nm size range agglomerated in secondary particles (Figure 2). The individual domains

TABLE 1 Unit cell parameters of the raw material and charged and first-cycle products.

Cell parameters	Raw material	After the first charge	After the first cycle
a (nm)	0.5099_3	0.4944_7	0.5061_6
b (nm)	0.2864_5	0.2931_6	0.2928_9
c (nm)	0.7130_3	0.7301_1	0.7104_1
β (°)	102.22_4	101.63_4	102.67_7
Cell volume (nm^3)	0.101_8	0.103_7	0.102_7

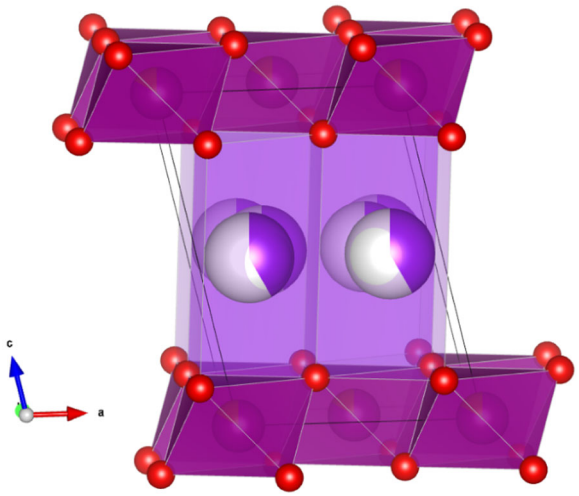

FIGURE 1 Refined structure of $K_{0.42}[Fe_{0.17}Mn_{0.83}]O_2$. O: small red spheres: K: large spheres, and Mn/Fe: intermediate spheres. (Mn, Fe)O_6 octahedra are dark purple and KO_6 trigonal prisms are light purple.

frequently showed (001) lattice fringes (Figure 2A), while the fourier transform (FT) of other HRTEM images could be indexed[11] according to the <010> zone axis (Figure 2B). These observations are in agreement with the structural parameters derived by XRD.

On the other hand, Figure 3 shows the Fe2p, Mn2p, O1s, and K2p regions of the XPS spectra of the raw sample. The Fe2p region shows two bands at 710.4 and 713.9 eV, as well as a satellite peak at 717.4 eV. These signals are ascribable to $Fe2p_{3/2}$ and $Fe2p_{1/2}$ levels of this transition metal in a trivalent oxidation state.[14] In the Mn2p region, the presence of asymmetric profiles agrees with the occurrence of two components ascribable to Mn^{3+} (641.3 and 651.8 eV) and Mn^{4+} (642.6 and 653.8 eV) as expected from the average oxidation state (3.7) for manganese in this sample.[15] Also, satellite peaks at 645.7 and 656.2 eV are observed. The O1s region shows a main signal at an asymmetric profile that can be decomposed into three components at 527.8 eV ascribable to the oxide atoms in the lattice as well as two additional lines at 530.8 and 533.6 eV arising from the surface oxide and carbonate species.[16] Finally, the presence of potassium is recognized by the $K2p_{1/2}$ and $K2p_{3/2}$ bands.

Due to the average oxidation state of Mn, in the 3+ to 4+ range, the material can be used starting with the charge or discharge of the cell. In the first case (Figure 4A), when charging up to 4.3 V, a capacity of 34 mAh g^{-1} is observed. The extraction is not complete since it represents 31% of the theoretical first charge capacity (109 mAh g^{-1} for full potassium extraction). This residual potassium in the structure may be favorable to maintaining the structural integrity of the compound, as suggested by Wang et al.,[4] for other compounds. In the XPS spectra of the charged electrodes, also shown in Figure 3, the oxidation of Fe^{3+} to Fe^{4+} and Mn^{3+} to Mn^{4+} is clear. On the other hand, there is a significant reduction in the intensity of the K2p signals after oxidation, which implies that it is only partially extracted from the network during cell charging.

Subsequently, the discharge of the cell is associated with the intercalation of sodium from the electrolyte. Thus, it is possible to intercalate more ions than the extracted K^+ ions during the charge, which leads to the partial reduction of Mn^{4+} to Mn^{3+}. This is evidenced in the CV plots in Figure 5A, which reveal two polarized reversible signals at 2.95/2.2 V (peaks 1/4) and 3.58/3.11 V (peaks 2/3) ascribable to iron and manganese redox pairs, respectively. The following cycles show a reversible capacity increasing from 60 to 80 mAh g^{-1}. This is maintained in this interval until 100 cycles. The stability suggests the pillaring effect of potassium[4,5] and its beneficial effect on structural stability. The initial increase in capacity can be attributed to further potassium extraction that does not suppress the pillaring effect, as it never reaches the theoretical 109 mAh g^{-1} corresponding to the complete potassium-pillars extraction. On the other hand, the curves at different kinetics (Figure 5B) show an interesting behavior up to the 2C rate, which may be associated with the greater interlayer separation in this compound, compared to similar sodium compounds.

To gain insight into the origin of the lattice stability of the studied compound upon cycling, ex situ XRD patterns were recorded after the first charge and after the first cycle (Figure S1). The unit cell parameters (Table 1) show a slight expansion in unit cell volume upon potassium extraction, mostly associated with changes in the a-parameter. The incomplete K-extraction prevents structural collapse. After the first cycle, there is a slight contraction again. However, the initial unit cell volume of the pristine compound is not recovered, thus indicating

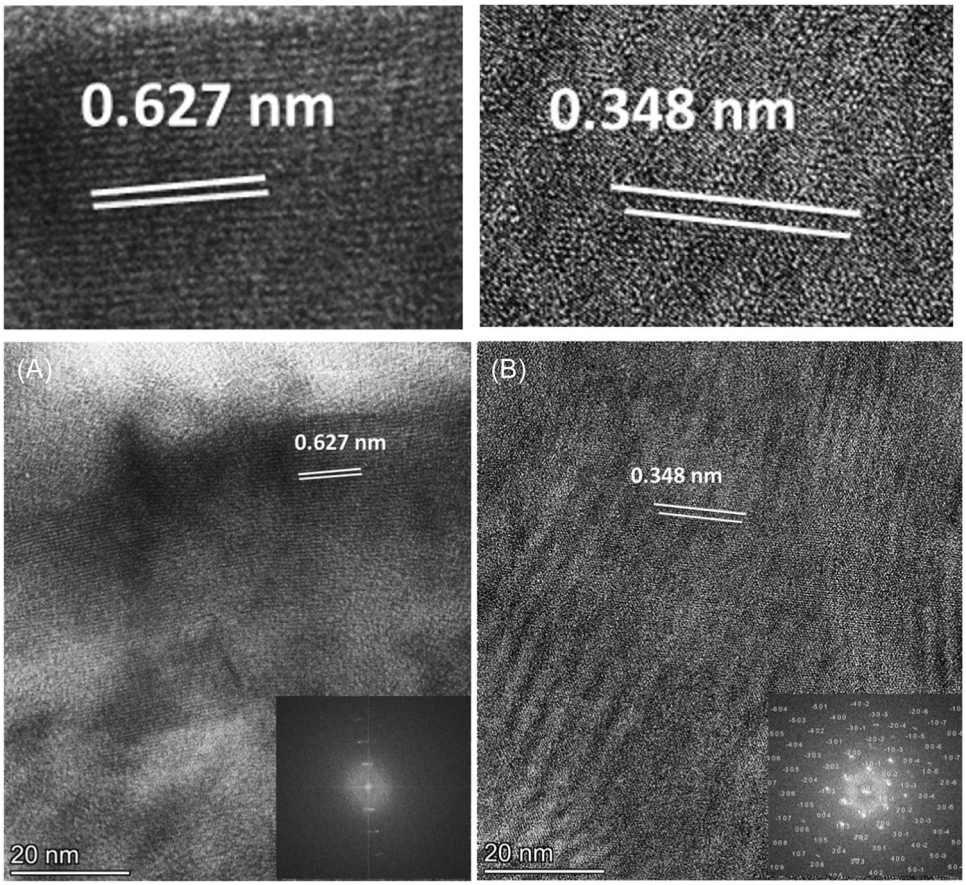

FIGURE 2 HRTEM of the $K_{0.42}[Fe_{0.17}Mn_{0.83}]O_2$. raw sample. (A) (001) lattice fringes. Inset: FT; (B) <010> zone axis. Inset: indexed FT. Top: magnified regions of the same images. HRTEM, high-resolution transmission electron microscopy.

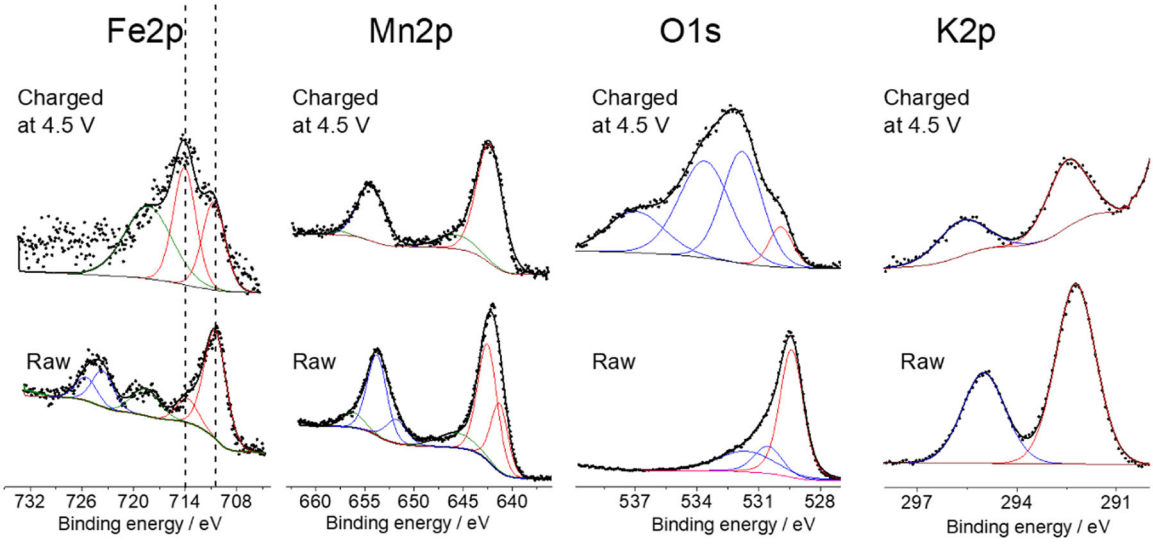

FIGURE 3 Fe2p, Mn2p, O1s, and K2p regions of the XPS of the raw sample and the sample charged at 4.5 V electrode.

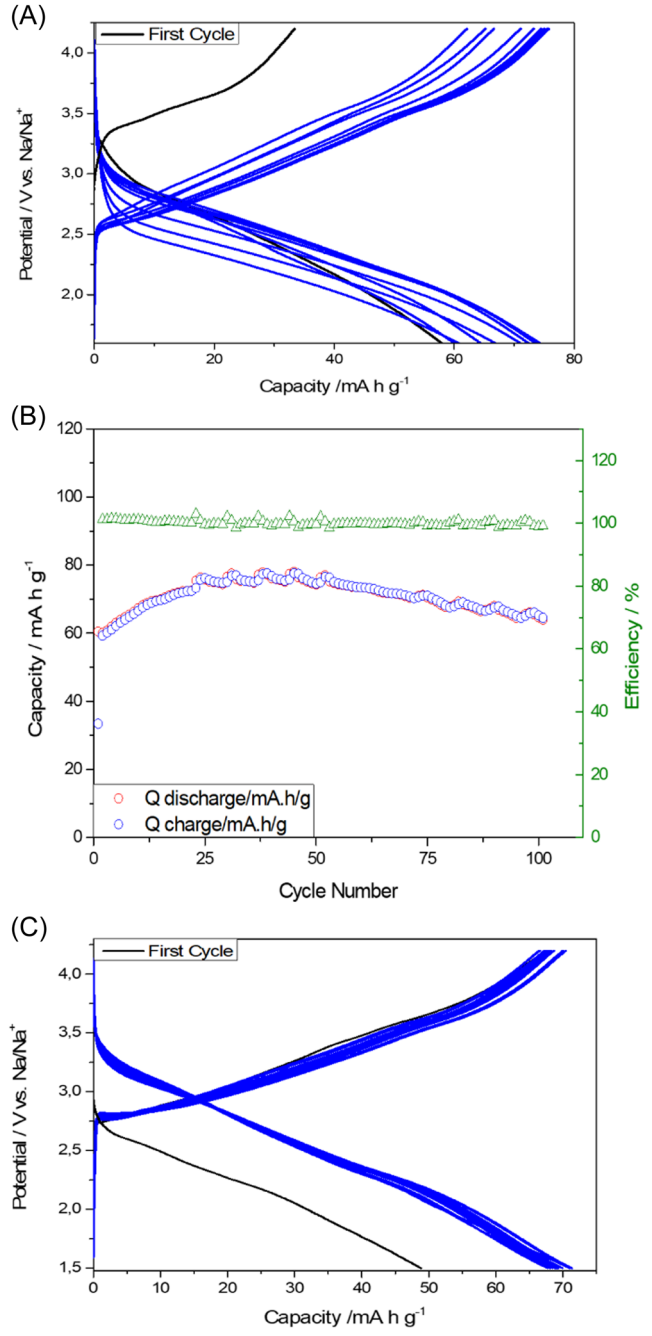

FIGURE 4 Galvanostatic cycling results for $K_{0.42}[Fe_{0.17}Mn_{0.83}]O_2$ electrodes in sodium half-cells at C/10, starting with (A, B) cell charge and (C) cell discharge.

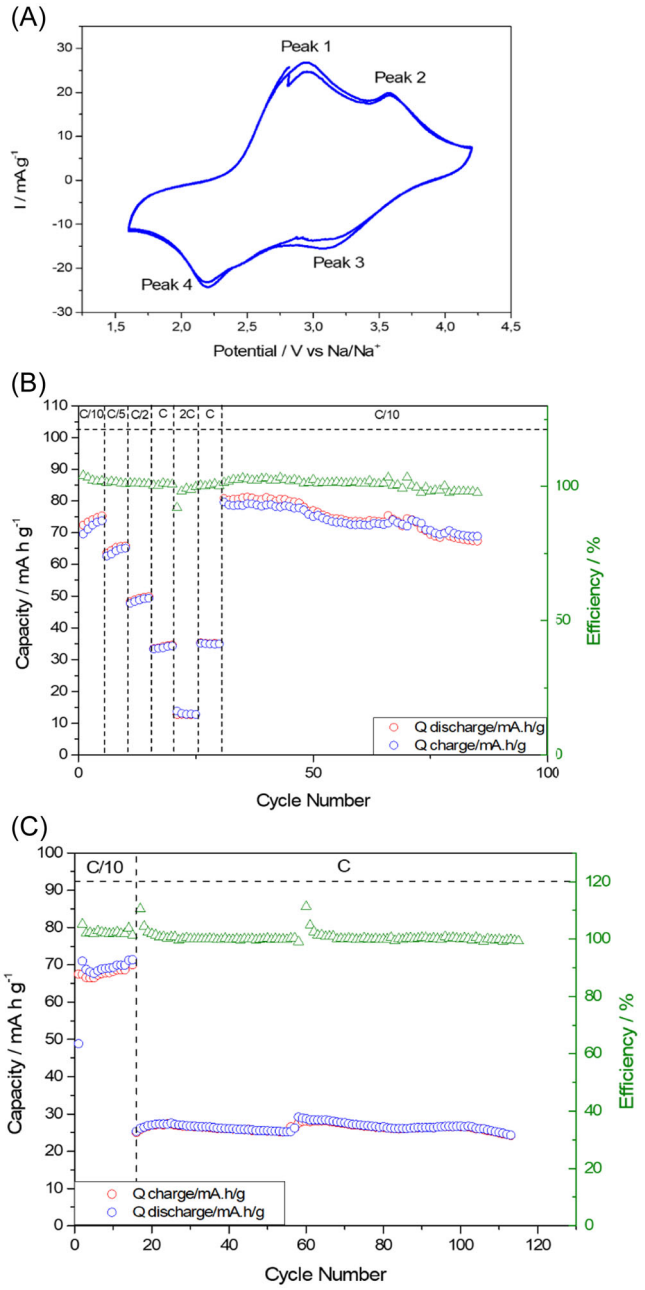

FIGURE 5 (A) First two CV cycles at 1 mV s^{-1}. Galvanostatic rate performance starting with charge (B) and discharge (C). CV, cyclic voltammetry.

the insertion of sodium during the first discharge. The overall changes are rather limited, thus allowing greater structural and mechanical stability of the cathode.

Figure 4B shows the electrochemical results starting with cell discharge. The performance in terms of capacity on cycling at C/10 is similar to the charge-starting experiments. Thus, the difference between the first and second discharge capacities is close to the first-charge capacity in Figure 4A. However, on increasing the rate to C (Figure 4A), there is a sharper decrease in capacity (Figure 5C). This means that the initial insertion of sodium could deteriorate the migration paths for sodium in the structure. A comparison of Figure 4A,C shows a progressive increase in capacity when starting with cell charge, while the test starting with charge provides a more constant capacity. The potassium extraction during the first charge opens a

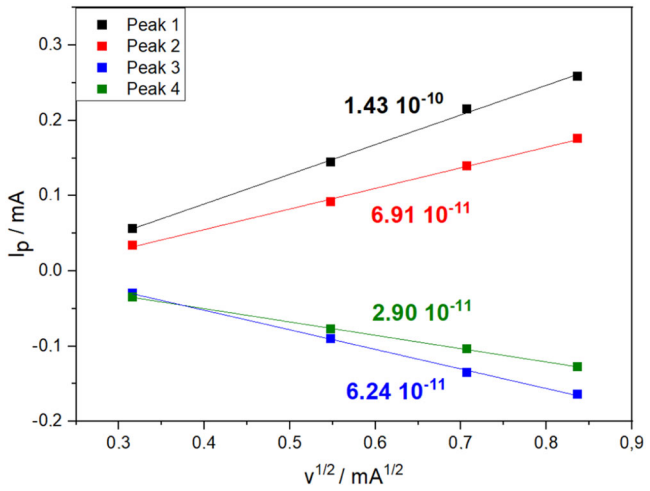

FIGURE 6 Plots of I_p versus $v^{1/2}$ from peaks 1–4 and 2–3 in Figure 5A for $K_{0.42}[Fe_{0.17}Mn_{0.83}]O_2$ electrodes.

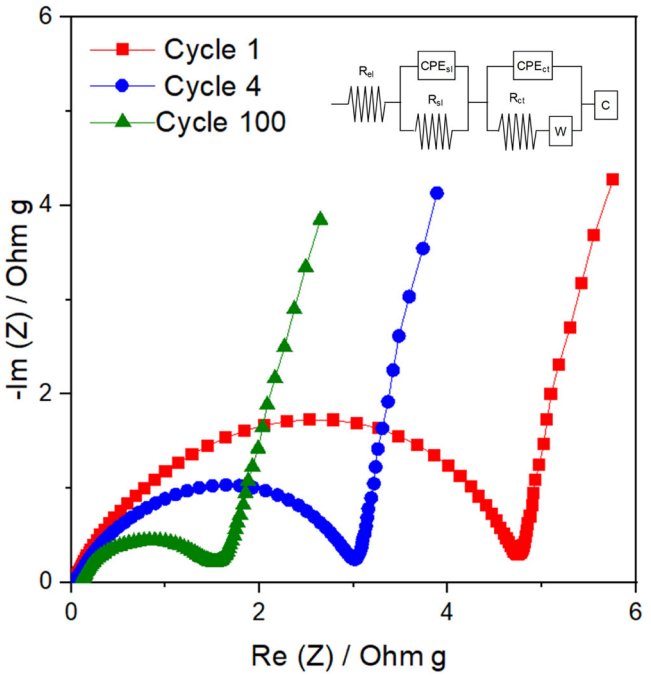

FIGURE 7 Nyquist plots obtained after the first four cycles and after cycle 100 for $K_{0.42}[Fe_{0.17}Mn_{0.83}]O_2$ electrodes. The equivalent circuit used in the analysis is also shown.

wide space for sodium insertion, as shown in Table 1, while the migration paths are filled with potassium when starting with cell discharge and impede increased capacities.

The analysis of CV curves at different rates (Figure S2) provided an estimation of the apparent sodium diffusion coefficients. Randles–Sevcik established that the diffusion coefficient ($D_{Na}+$) can be calculated when their current intensity maxima (I_p) are proportional to the square root of the sweep rate ($v^{1/2}$) according to the following equation[17,18]:

$$D_{Na^+} = 2.69 \cdot 10^{-5} n^{3/2} S^{1/2} C v^{1/2}, \quad (1)$$

where n is the number of electrons transferred in the redox reaction, S is the geometric area of the electrode, and C is the bulk concentration of electroactive Na^+.

Figure 6 shows the linearity of these plots for both anodic and cathodic peaks of $K_{0.42}[Fe_{0.17}Mn_{0.83}]O_2$ electrodes. From their slopes, the sodium diffusion coefficients ($D_{Na}+$) were calculated, and these values are also shown in Figure 6. These results reveal that sodium diffusion is faster during the oxidation–reduction of Mn than during the changes in the oxidation state of iron. In addition, the numerical values compare well with other reports in the literature for both sodium[3] and potassium[4] batteries.

On the other hand, the Nyquist plots shown in Figure 7 were obtained from EIS after successive cycles and after prolonged cycling at 300 mA g^{-1}. These plots showed two semicircles at high and medium frequencies that could be fitted to the equivalent circuit shown as an inset in Figure 7. The fitting results presented in Table S2 include the electrolyte resistance (R_{el}), the cell internal resistances at the surface layer (R_{sl}), and the charge-transfer resistance (R_{ct}) at the electrode–electrolyte interphase. First, the R_{el} is low as usual for liquid electrolyte cells. The values of R_{sl} and R_{ct} decrease progressively after the extended cycling, which agrees well with the rate performance and apparent diffusion coefficients described above.

Finally, the apparent diffusion coefficients $D_{Na}+$ can also be determined from the impedance spectra. According to Equation (2), the apparent diffusion coefficients can be expressed as[19]:

$$D_{Na^+} = 0.5(RT/SF^2\sigma_\omega C)^2, \quad (2)$$

where R is the gas constant, T is the absolute temperature, F is Faraday's constant, and C is the molar concentration of Na^+ ions in the formula unit. The Warburg coefficient (σ_ω) can be deduced from the slope of the linear segment of the real impedance (Z') when plotted versus the reciprocal square root of the lower angular frequencies ($\omega^{-1/2}$), as shown in Figure S3. From these plots, a negligible variation in slope, and thus, in the apparent diffusion coefficients, can be observed when the cycle number increases, which confirms the high stability of the studied material, also in agreement with the CV

determinations and the structural stability revealed by the XRD analysis.

4 | CONCLUSIONS

In this work, the results corresponding to the layered compound P′3-$K_{0.42}[Fe_{0.17}Mn_{0.83}]O_2$ are presented. It was prepared using a sol–gel procedure that yielded a product with relatively high purity, with an indexable structure in the C2/*m* space group of the monoclinic system ($a = 0.5099_3$ nm, $b = 0.2864_5$ nm, $c = 0.7130_3$ nm y $\beta = 102.22_4°$). Manganese in the 3.7+ oxidation state avoids a high negative incidence of the dynamic Jahn–Teller effect. Its electrochemical behavior was tested in sodium metal half-cells using $NaClO_4$ in PC and FEC (98:2) as the electrolyte. When the cell is charged up to 4.3 V, it is observed that the potassium extraction is not complete. Residual potassium in the structure may be favorable for maintaining the structural integrity of the compound. The subsequent discharge of the cell is associated with the intercalation of sodium from the electrolyte. Thus, it is possible to incorporate a greater number of alkaline ions than those extracted in the previous charge, which leads to a decrease in the initial average state. The following cycles show a reversible capacity increasing from 60 to 80 mAh g^{-1} and excellent cyclability. This can be explained by the beneficial effect of potassium, which would act as a structural "pillar" in the interlayer, which would reduce structural degradation during cycling. On the other hand, the curves at different kinetics show an interesting behavior at kinetics up to 2C, associated with the greater interlaminar separation in this compound, compared to similar sodium compounds.

ACKNOWLEDGMENTS

The authors are grateful for the funding of the project PLEC2021-007779 entitled "Electrolytes and innovative electrodes for a new generation of sodium batteries for stationary applications (NABASTAT)," financed by MCIN/AEI/10.13039/501100011033 and by the European Union "NextGenerationEU" /PRTR, and the Junta de Andalucía (group FQM288), IQUEMA, and SCAI (UCO).

CONFLICT OF INTEREST STATEMENT

The authors declare no conflict of interest.

DATA AVAILABILITY STATEMENT

The data that support the findings of this study are available from the corresponding author upon reasonable request.

ORCID

José L. Tirado http://orcid.org/0000-0002-8317-2726

REFERENCES

1. Han MH, Gonzalo E, Singh G, Rojo T. A comprehensive review of sodium layered oxides: powerful cathodes for Na-ion batteries. *Energy Environ Sci*. 2015;8:81-102.
2. Zuo W, Innocenti A, Zarrabeitia M, Bresser D, Yang Y, Passerini S. Layered oxide cathodes for sodium-ion batteries: storage mechanism, electrochemistry, and techno-economics. *Acc Chem Res*. 2023;56:284-296.
3. Wang PF, You Y, Yin YX, Guo YG. Layered oxide cathodes for sodium-ion batteries: phase transition, air stability, and performance. *Adv Energy Mater*. 2018;8:1701912.
4. Wang Y, Feng Z, Cui P, et al. Pillar-beam structures prevent layered cathode materials from destructive phase transitions. *Nat Commun*. 2021;12:13.
5. Wang X, Hu P, Niu C, et al. New-type $K_{0.7}Fe_{0.5}Mn_{0.5}O_2$ cathode with an expanded and stabilized interlayer structure for high-capacity sodium-ion batteries. *Nano Energy*. 2017;35:71-78.
6. Mortemard de Boisse B, Carlier D, Guignard M, Bourgeois L, Delmas C. P2-$Na_xMn_{1/2}Fe_{1/2}O_2$ phase used as positive electrode in Na batteries: structural changes induced by the electrochemical (de)intercalation process. *Inorg Chem*. 2014;53:11197-11205.
7. Liu C, Luo S, Huang H, Liu X, Zhai Y, Wang Z. Fe-doped layered P3-type $K_{0.45}Mn_{1-x}Fe_xO_2$ ($x \leq 0.5$) as cathode materials for low-cost potassium-ion batteries. *Chem Eng J*. 2019;378:122167.
8. Wang S, Sun T, Yuan S, et al. P3-type $K_{0.33}Co_{0.53}Mn_{0.47}O_2$·0.39-$H_2O$: a novel bifunctional electrode for Na-ion batteries. *Mater Horiz*. 2017;4:1122-1127.
9. Wang C, Liu L, Zhao S, et al. Tuning local chemistry of P2 layered-oxide cathode for high energy and long cycles of sodium-ion battery. *Nat Commun*. 2021;12:2256.
10. Gupta P, Pushpakanth S, Haider MA, Basu S. Understanding the design of cathode materials for Na-ion batteries. *ACS Omega*. 2022;7:5605-5614.
11. Klinger M, Jäger A. Crystallographic Tool Box (CrysTBox): automated tools for transmission electron microscopists and crystallographers. *J Appl Crystal*. 2015;48:2012-2018.
12. Kumakura S, Tahara Y, Sato S, Kubota K, Komaba S. P′2-$Na_{2/3}Mn_{0.9}Me_{0.1}O_2$ (Me = Mg, Ti, Co, Ni, Cu, and Zn): correlation between orthorhombic distortion and electrochemical property. *Chem Mater*. 2017;29:8958-8962.
13. Naveen N, Han SC, Singh SP, Ahn D, Sohn KS, Pyo M. Highly stable P′3-$K_{0.8}CrO_2$ cathode with limited dimensional changes for potassium ion batteries. *J Power Sources*. 2019;430:137-144.
14. Zhou D, Zeng C, Ling D, et al. Sustainable alternative cathodes of sodium-ion batteries using hybrid P_2/O_3 phase $Na_{0.67}Fe_{0.5}Mn_{0.5-x}Mg_xO_2$. *J Alloys Compd*. 2023;931:167567.
15. Yuan D, Hu X, Qian J, et al. P2-type $Na_{0.67}Mn_{0.65}Fe_{0.2}Ni_{0.15}O_2$ cathode material with high-capacity for sodium-ion battery. *Electrochim Acta*. 2014;116:300-305.
16. Siriwardena DP, Fernando JFS, Wang T, et al. $Na_{0.67}Mn_{(1-x)}Fe_xO_2$ compounds as high-capacity cathode materials for rechargeable sodium-ion batteries. *ChemElectroChem*. 2021;8:508-516.
17. Randles JEB. A cathode ray polarograph. Part II—the current-voltage curves. *Trans Faraday Soc*. 1948;44:327-338.
18. Ševčík A. Oscillographic polarography with periodical triangular voltage. *Collect Czech Chem Commun*. 1948;13:349-377.
19. Shenouda AY, Liu HK. Preparation, Characterization, and electrochemical performance of Li_2CuSnO_4 and $Li_2CuSnSiO_6$

electrodes for lithium batteries. *J Electrochem Soc*. 2010;157: A1183-A1187.

SUPPORTING INFORMATION

Additional supporting information can be found online in the Supporting Information section at the end of this article.

How to cite this article: Aranda M, Lavela P, Tirado JL. A novel potassium-containing layered oxide for the cathode of sodium-ion batteries. *Battery Energy*. 2024;20230057. doi:10.1002/bte2.20230057